Energy Reports 10 (2023) 837–849

Contents lists available at ScienceDirect

Energy Reports

journal homepage: www.elsevier.com/locate/egyr

Cost-effective microwave-assisted O3- type sodium-based layered oxide cathode materials for sodium-ion batteries

R.A. Harindi Gayara [a,b], Buzaina Moossa [a,c], R.A. Shakoor [a,d,*], Rana Faisal Shahzad [e], Muhammad Sajjad [f], Nirpendra Singh [f], Shahid Rasul [e], Talal Mohammed Al tahtamouni [b]

[a] Center for Advanced Materials (CAM), Qatar University, P.O. Box 2713, Doha, Qatar
[b] Materials Science and Technology program, College of Art & Sciences, Qatar University, P.O. Box 2713, Doha, Qatar
[c] Department of Chemical Engineering, College of Engineering, Qatar University, P.O. Box 2713, Doha, Qatar
[d] Department of Mechanical and Industrial Engineering, College of Engineering, Qatar University, P.O. Box 2713, Doha, Qatar
[e] Faculty of Engineering and Environment, Northumbria University, Ellison Pl, Newcastle Upon Tyne, NE1 8ST, UK
[f] Khalifa University, P.O. Box: 127788, Abu Dhabi, United Arab Emirates

ARTICLE INFO

Article history:
Received 25 April 2023
Received in revised form 7 July 2023
Accepted 18 July 2023
Available online 28 July 2023

Keywords:
Sol–gel
O3-type layered oxide
Cathode materials
Sodium-ion battery
Energy storage

ABSTRACT

In this work, phase pure and highly crystalline O3-type layered oxide material ($Na_1Ni_{0.33}Mn_{0.33}Fe_{0.33}O_2$-NNMF) was developed using; (i) a conventional solid-state synthesis route and (ii) a facile microwave-assisted sol–gel technique. A comparison of structural, thermal, and electrochemical properties is presented to elucidate the usefulness of the microwave-assisted sol–gel synthesis technique. A remarkable reduction in the sintering process time is noticed in the microwave-assisted sol–gel synthesis technique without compromising on the structural, thermal and electrochemical properties when compared to the conventional solid-state synthesis route confirming its decent cost-effectiveness. It is further noticed that NNMF developed through microwave-assisted sol–gel synthesis technique demonstrates superior thermal stability and comparable electrochemical performance as compared to the same material produced through the conventional sintering process. The decent electrochemical properties induced in NNMF during the microwave-assisted sol–gel synthesis technique can be attributed to the efficient diffusion of Na^+ ions into/from the host structure during the intercalation/de-intercalation process as indicated by the high value of sodium diffusion coefficient (1×10^9-3.58×10^9 $m^2\,s^{-1}$). The Potentiostatic Intermittent Titration Technique (PITT) analysis confirms single-phase Na^+ intercalation/deintercalation in the host structure, regardless of the synthesis process. Finally, EIS analysis confirms the capacity fading of the developed materials during the cycling process is essentially due to an increase in the resistance with the increasing number of cycles due to the gradual thickening of formed SEI layer. The microwave-assisted sol–gel synthesis technique can be effectively employed for the production of many families of cathode materials at competitive cost facilitating their commercialization.

1. Introduction

Unprecedented energy shocks and crises are disrupting energy systems, and there is an urgent need to reconcile energy security, equality, and environmental sustainability. Energy Security assesses a country's ability to meet current and future energy demands, while energy equity measures access to affordable energy. Environmental sustainability assesses the energy system performance of a country in preventing environmental damage and mitigating climate change (World Energy Council, 2022; Gür, 2018; Leurent, 2023). Renewable energy sources such as hydroelectric, biomass, wind, nuclear, solar energy, and grid energy storage are being developed due to the energy limitation. As an example, nuclear reactions have disadvantages such as high cost, wastage of radioactive components and adverse effects on human health and safety. Renewable energy sources allow consumption over a long period with minimal environmental impact (Liu et al., 2016). Concerns about adverse impacts on biodiversity, climate change, increasing environmental degradation, and global temperature instability has led to the development of alternative energy resources, renewables, and electric storage technologies (Yang, 2011; Goodenough and Kim, 2010; Hirsh et al., 2020).

Batteries with high energy density can be used for grid storage and automobiles (Wang et al., 2020). Lithium-ion Batteries

* Corresponding author at: Center for Advanced Materials (CAM), Qatar University, P.O. Box 2713, Doha, Qatar.
E-mail addresses: shakoor@qu.edu.qa (R.A. Shakoor), taltahtamouni@qu.edu.qa (T.N. Al tahtamouni).

https://doi.org/10.1016/j.egyr.2023.07.038

(LIBs) are becoming increasingly popular in grid applications and electric vehicle deployments due to their superior coulombic efficiency, structural integrity and power density (Mizushima et al., 1980; Yazami and Touzain, 1983; Thackeray et al., 1983; Lu et al., 2001). The widespread use of LIBs has raised questions regarding the availability and price of lithium and other transition metals required for lithium-ion technology, such as nickel and cobalt, prompting the development of alternative sustainable battery technologies (Diouf and Pode, 2015; Ge and Fouletier, 1988; Yabuuchi et al., 2012a). Na-ion batteries (SIBs) have reemerged as a viable alternative or in addition to LIBs due to their low cost and excellent sustainability prospects (Whittingham, 1978). Despite their inherent disadvantage in energy density, SIBs still appear promising for large-scale energy storage, where the cost ($ per kW) and lifetime (years, number of cycles) are the most critical factors. Li-ion chemistry research experiences have helped the SIB technology advance effectively, producing successful research results (Chayambuka et al., 2020).

Therefore, SIBs with superior cycling ability and lower volumetric energy density can be used for grid energy storage. Due to iron's (Fe) availability and low cost, iron-based cathode materials are of particular interest. Fe^{3+} and Li^{+} cations in lithium iron oxides combine more frequently than Fe^{3+} and Na^{+} ions (Tanaka et al., 2009). According to studies, the P2-phase of $Na_{0.67}Fe_{0.5}Mn_{0.5}O_2$ has an energy density of more than 500 Wh/kg while utilizing some of the world's most inexpensive and readily available materials. This is a positive step forward for long-lasting high energy density battery chemistries. Layered Na-ion cathode materials with energy densities ranging from 1100 to 1800 Wh/L (275 to 375 Wh/kg) have been studied, including $NaVO_2$, $NaCrO_2$ (Komaba et al., 2010), $NaNi_{0.5}Mn_{0.5}O_2$ (Komaba et al., 2012), and $NaFe_{0.33}Mn_{0.33}Ni_{0.33}O_2$ (Kim et al., 2012). Higher energy densities of around 2000 Wh/L (500 Wh/kg) have been achieved using $NaNi_{0.33}Mn_{0.33}O_2$ (Yabuuchi and Komaba, 2014), $NaMnO_2$ (Ma et al., 2011), and P3-$NaCoO_2$ materials compared to $LiCoO_2$'s 3000 Wh/L, while considerable capacity retention has not been confirmed.

Numerous other potential P2 and O-type layered Na_xMO_2 cathodes for Na-ion batteries have been reported (Pan et al., 2013), including P2-Na_xCoO_2 (Berthelot et al., 2011; Pan et al., 2013; Ding et al., 2013), $Na_xMn_yCo_{1-y}O_2$ (Paulsen and Dahn, 1999; Wang et al., 2013; Carlier et al., 2011), O3- or P2-$Na_xFe_{0.5}Mn_{0.5}O_2$ (Yabuuchi et al., 2012b) and Na_x $MnyFe_{1-y}O_2$ (Sendova-Vassileva et al., 2010; Mortemard de Boisse et al., 2013; Thorne et al., 2014), Fe-containing O3- $NaFe_{0.5}Co_{0.5}O_2$ (Yoshida et al., 2013), $NaFe_yNi_{1-y}O_2$ (Wang et al., 2014), $NaNi_{0.33}Co_{0.33}Fe_{0.33}O_2$ (Kalluri, 2016), and $NaNi_{0.33}Mn_{0.33}Fe_{0.33}O_2$ (Kim et al., 2012); and various $Na_xFe_yMn_{1-y-z}Ni_zO_2$ compound (Yabuuchi et al., 2013; Yuan et al., 2014). Na P2-type layered transition metal oxide with $Na_{1.0}Li_{0.2}Ni_{0.25}Mn_{0.75}O_2$ has been reported in metallic Na cells with good battery performance as the layered architectures of Na transition metal oxides allow for reversible Na intercalation (Kubota et al., 2014). Electrochemical reversibility was demonstrated in a single intercalated layered phase with a minimal crystal volume change and a delta stoichiometry of 0.42 Na.

In this work, layered Na $(Ni_{0.33}Mn_{0.33}Fe_{0.33})$ O_2 was synthesized by including Fe and readjusting the mole stoichiometry of Ni and Mn in $NaNi_{0.5}Mn_{0.5}O_2$ base material. This electrode will have a larger capacity and lower material costs due to more redox active Ni (1/3>1/4) (Yang et al., 2018). Developing innovative electrode materials (Hoseinzadeh et al., 2017) that can be mass-produced to promote the industrialization of sodium-ion batteries is essential. Adopting simple, controllable, low-cost, and low-emission synthesis techniques for industrial manufacturing is more preferred in terms of saving time, money and energy spent on for abundant sodium-based cathode materials production (Wang et al., 2016). Because of its unique heating mechanism, microwave sintering is a relatively new synthesis approach with a concise synthesis time (Suryakala et al., 2007; Kebede et al., 2017; Burova et al., 2019). Unfortunately, there are only a few reports on using microwave sintering to synthesize electrode materials (Bomio et al., 2022; Mohanty et al., 2018; Bomio et al., 2023; Yamada et al., 2007; Qureshi et al., 2022). The typical microwave sintering cycle operates at a low temperature and requires only 80 minutes of dwell time, which is extremely short compared to traditional sintering approaches (10–12 h), specifically for NNMF material. The major challenge, however, is the synthesis of the impurity-free phase. Nonetheless, this simple, cost-effective microwave-assisted sol–gel technique can benefit economically synthesizing electrode materials for battery technology with improved electrochemical performance and proper understanding and engineering of the process. Herein, we report the efficient use of the microwave-assisted sol–gel process to create O3-type $Na_1Ni_{0.33}Mn_{0.33}Fe_{0.33}O_2$ and examine the material's cycle performance. The operating voltage range of 2.0V–4.0 V significantly influences the cycling performance of this material. We add inexpensive iron ions (Fe^{2+}) to the $NaNi_{0.5}Mn_{0.5}O_2$ crystal structure, facilitating the transition to outstanding structural stability and high reversible capacity. One factor that has considerably influenced the reversible capacities is the Fe^{2+}/Fe^{3+} redox, particularly when charging to a high cutoff voltage, and the significant improvement in cycle reversibility, a known method of preventing the upper voltage phase transition (Kim et al., 2012).

2. Materials and methods

2.1. Material synthesis

The precursors of CH_3 COONa (ACS.VWR Chemicals), Ni $(CH_3COO_2).4H_2O$ (Sigma Aldrich), Mn $(CH_3COO_2).4H_2O$ (Carl-Roth GmbH.Co) and Fe $(CH_3COO_2).4H_2O$ (Sigma Aldrich) were used to synthesize $Na_1Ni_{0.33}Mn_{0.33}Fe_{0.33}O_2$ (NNMF) via the sol–gel method. Appropriate amounts of the above chemicals were used as the starting material for the $Na_1Ni_{0.33}Mn_{0.33}Fe_{0.33}O_2$ synthesis in the de-ionized aqueous medium. As a chelating agent, Citric Acid (Sigma Aldrich) was added 0.3 times the total quantity of transition metals.

The sample mixture proceeded with 15–30 min of homogeneous stirring at a 300-rpm stirring rate. The mixture temperature was heated to 85 °C overnight (∼ 12 h). The formed sol–gel completely dried at 120 °C for 5 h in the vacuum drying oven (Biobase Biodustry). The dried sample was ground using a mortar and pestle to a fine powder and formed pellets using the hydraulic press (Caver, INC) to perform the calcination process as shown in Fig. 1 (a) and (b).

2.2. Sintering categories

Conventional Sintering (NNMF-CS).

The sample pellet was placed in an alumina crucible, and calcination proceeded in two heat treatment process; heat treatment 01 (HT 01) at 350 °C for 3 h and heat treatment 02 (HT 02) where the atmospheric condition at 800 °C for 12 h (Kim et al., 2012) using a Muffle furnace (Nabertherm 3000). The calcined sample was ground into fine powder for further characterization as illustrated in Fig. 1(a).

Microwave Sintering (NNMF-MW).

The calcination was undergone similarly as NNMF-CS with HT 01 at 350 °C for 3 h using a Muffle furnace (Nabertherm 3000) and HT 02 at 800 °C for 80 min using the VBCC Hytherm Microwave furnace (VB Ceramic) with 2.45 GHz of the magnetron 1 °C accuracy at dwell temperature as illustrated in Fig. 1(b).

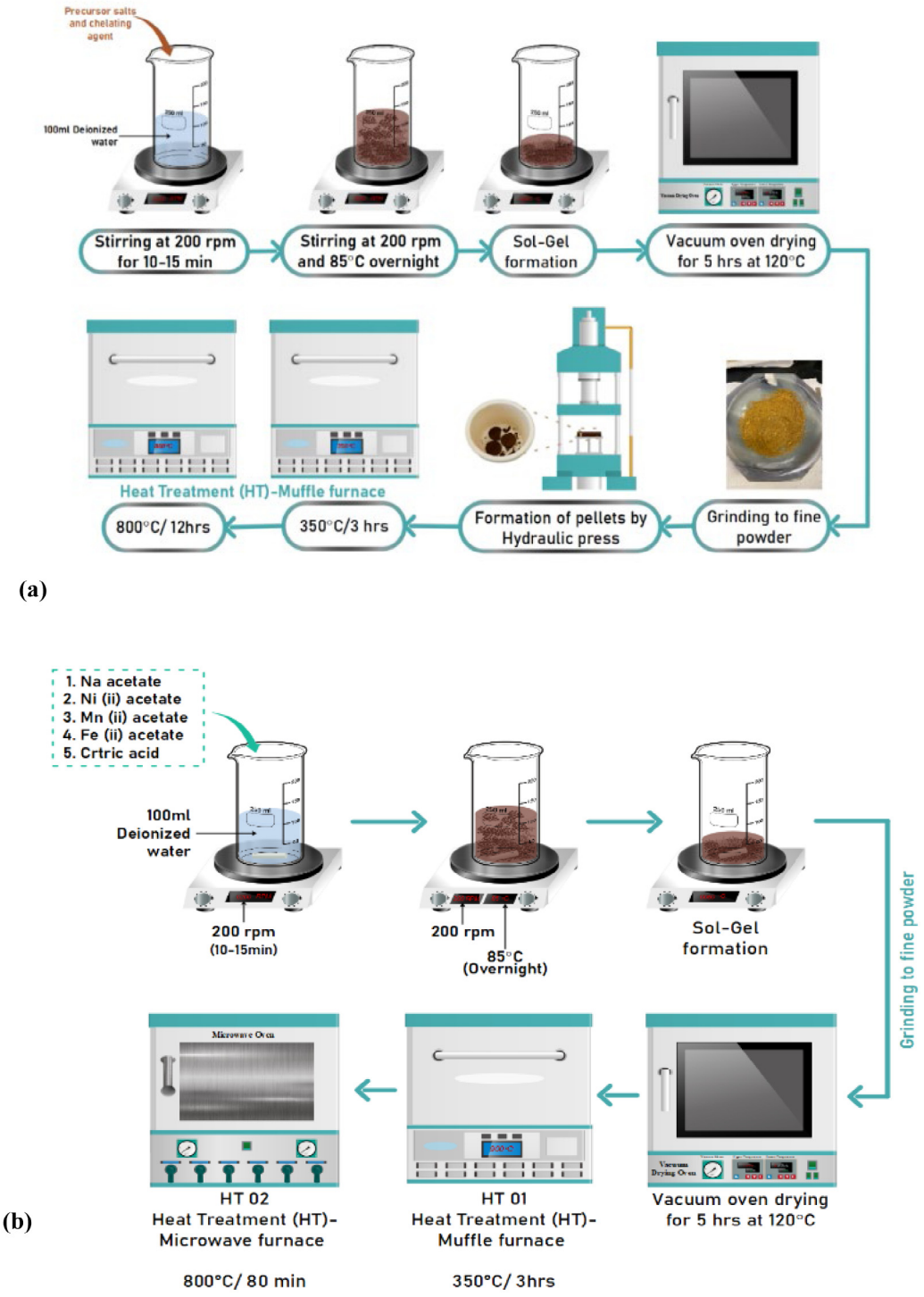

Fig. 1. Schematic illustration of the synthesis process for $Na_1Ni_{0.33}Mn_{0.33}Fe_{0.33}O_2$ cathode material with two different sintering techniques. (a) Synthesis through conventional sintering method calcination under atmospheric conditions. (b) Heat treatment under microwave sintering.

2.3. Electrochemical cell fabrication

To determine the electrochemical performances, sintered samples of $Na_1Ni_{0.33}Mn_{0.33}Fe_{0.33}O_2$ a slurry medium was prepared as to the ratio of 80:10:10 of active material, activated carbon and PVDF (Polyvinyl difluoride) using NMP (N-methyl-2-pyrrolidone) solvent. The prepared mixtures (slurry) were stirred overnight for a homogeneous mixture. Moreover, the mixture was coated on battery-grade Al (Aluminum) foil for cathode material. The coated foil was vacuum dried (*Biobase Biodustry (Shandong) Co., Ltd China*) for 4 h and was calendered using electric precision width rolling press (MTI Corporation, USA) then punched with a compact precision press and ring cutter (MIT Corporation, USA Model: T07) to obtain 14 mm(diameter) electrodes. The sample electrodes were vacuum dried for another 2 h and placed inside an argon-filled glovebox (LC Technology Solutions Inc. (Salisbury, USA) LC-100 Retch PM 200). The coin CR-2032 type cells were used to prepare Na half-cells. Sodium (Na) metal was used as an anode, 1M Sodium perchlorate ($NaClO_4$) in propylene carbonate (PC) was used as an electrolyte, and Whatman glass fiber

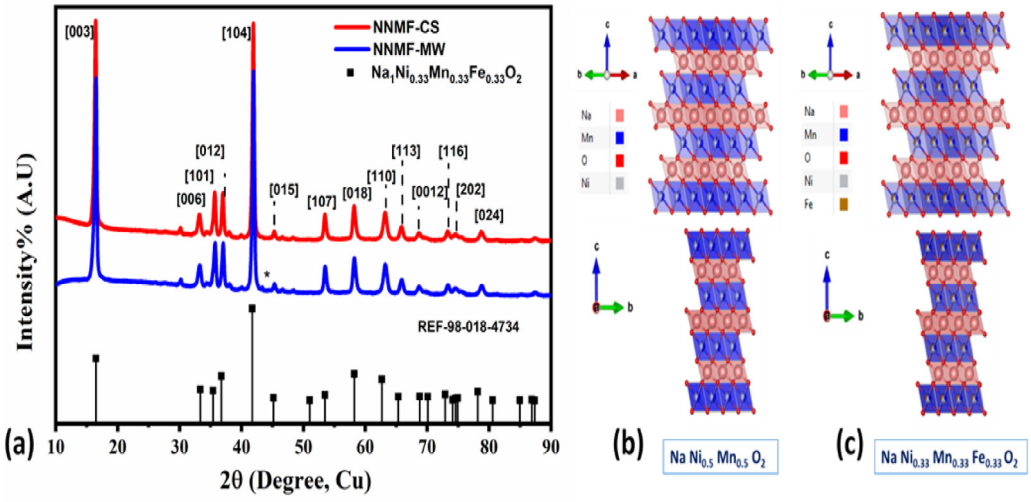

Fig. 2. (a) XRD Spectrum representing the conventionally sintered and microwave sintered $Na_1Ni_{0.33}Mn_{0.33}Fe_{0.33}O_2$ material and the comparison between the reference pattern. (b) Structure of the $Na_1Ni_{0.5}Mn_{0.5}O_2$ base material and the (c) shows the iron incorporated $Na_1Ni_{0.33}Mn_{0.33}Fe_{0.33}O_2$ material structure.

as the 20 mm (diameter) separator. The battery cycle system (WBCS 3000L WonTech Co., Ltd) was used to cycle the Na half cells/Na/Na^+ in a range of 2.0V–4.0 V.

2.4. Structural characterization

X-ray diffraction (XRD) measurements for the NNMF-CS and NNMF-MW cathode materials were carried out using a scan range of 10–100 values of 2θ, the K-Alpha wavelength ratio of 0.5 and Cu anode material consisting of an X-ray diffractometer (PANalytical EMPYREAN). The variety of sintered materials was subjected to overnight slow-rate scanning in 10–120 for detailed diffraction spectrum analysis. SEM/EDAX analysis to obtain the surface morphology and sample topological analysis was carried out using a Scanning electron microscope (SEM)-(Nova Nano SEM 450) and Energy dispersive X-ray analysis (EDAX-Bruker) detector to analyze the elemental distribution. Transmission electron microscope (TEM)-(FEI TECNAI G2 TEM, TF20) was used to determine the structural distribution, grain size and lattice fringes, obtain high-resolution TEM images of the cathode materials. Thermal gravimetric analysis (TGA) & DSC thermal stability data were conducted using Thermogravimetric Analyzer (Perkin Elmer Pyris 6) and Differential scanning calorimeter (214 Polyma NETZSCH) to obtain the studies of the sample stability to oxidation. Raman spectroscopic details**;** The vibrational spectroscopic data were collected using a Thermo fisher scientific DXR Raman Microscope with a wavelength of 532 nm, 40 times scan, and the laser power is 10 using 50X microscope objectives. Fourier transform-infrared spectroscopic (FT-IR) details correspondent to the high-spectral-resolution data was obtained over a wide spectral range in 400–4000 cm^{-1}, using Perkin Elmer (Spectrum 400) FT-IR spectrometer.

2.5. Electrochemical characterization

The battery cycle system (WBCS 3000L WonTech Co., Ltd) was used to cycle the Na half cells/Na/Na^+ in a range of 2.0 V - 4.0 V. The electrochemical analysis methods, namely the galvanostatic intermittent titration technique (GITT) 0.1C, cyclic voltammetry (CV), potentiostatic intermittent titration technique (PITT), galvanostatic charge–discharge (GCD), and rate capability (RC) were performed on the cells at room temperature.

Table 1
Value of the lattice parameter a for sol–gel synthesized NNMF-CS and NNMF-MW.

Material	a (A°)	b (A°)	c (A°)	Volume $(A°)^3$
O3- NNMF-CS	2.89095	2.89095	16.02511	115.9881
O3- NNMF-MW	2.89077	2.89077	15.9947	115.7538

3. Results and discussion

The structural analysis results shows that all Braggs peaks can be assigned to the hexagonal closed-packed structure in space group $\bar{R}3$ m. Fig. 2(a) presents the XRD patterns of the microwave-sintered $Na_1Ni_{0.33}Mn_{0.33}Fe_{0.33}O_2$ (NNMF-CS) material in red and NNMF-MW in blue. Fig. 2(b) and (c) represent the structure of the O3-type $Na_1Ni_{0.5}Mn_{0.5}O_2$ and $Na_1Ni_{0.33}Mn_{0.33}Fe_{0.33}O_2$, respectively. The peaks of the XRD patterns are well indexed with ref-98-018-4734 of prior work (Kim et al., 2012). The presence of clear and sharp peaks in the XRD spectra indicates the high purity and crystallinity of the synthesized materials. Previous research employed a solid-state technique with a standard sintering period of 12 h at 850 °C for the NNMF material. The ability of the microwave sintering method to produce phase-pure NNMF material is demonstrated by the similarity of the diffraction peaks present in the XRD spectra of the same material produced using the conventional sintering approach, as shown in Fig. 2(a).

Table 1 Displays the lattice parameter "a" for NNMF-CS and NNMF-MW materials. The little differences in the lattice parameter values suggest that the structure of the materials generated is not significantly affected by additional heat treatment in the microwave furnace. However, the lattice parameter (c) of NNMF-MW is slightly smaller than that of NNMF-CS, being 16.025 (c = 15.994). This has an effect on sodium-ion transport, which is slightly more complicated when compared to a molecule with a bigger particle size. This can be achieved by stoichiometry, which incorporates a considerable quantity of sodium.

SEM/EDAX images of the NNMF-CS and NNMF-MW samples are shown in Fig. 3. Figs. 3(a) and 3(b) demonstrate the presence of the precursor transition metal ions and the successful formation of layered oxide cathode materials from EDAX images. Fig. 3(c) shows SEM images of NNM-CS with a slab-like layered structure with soft edges and small particles agglomerated around it. It can be considered smaller slab particles of

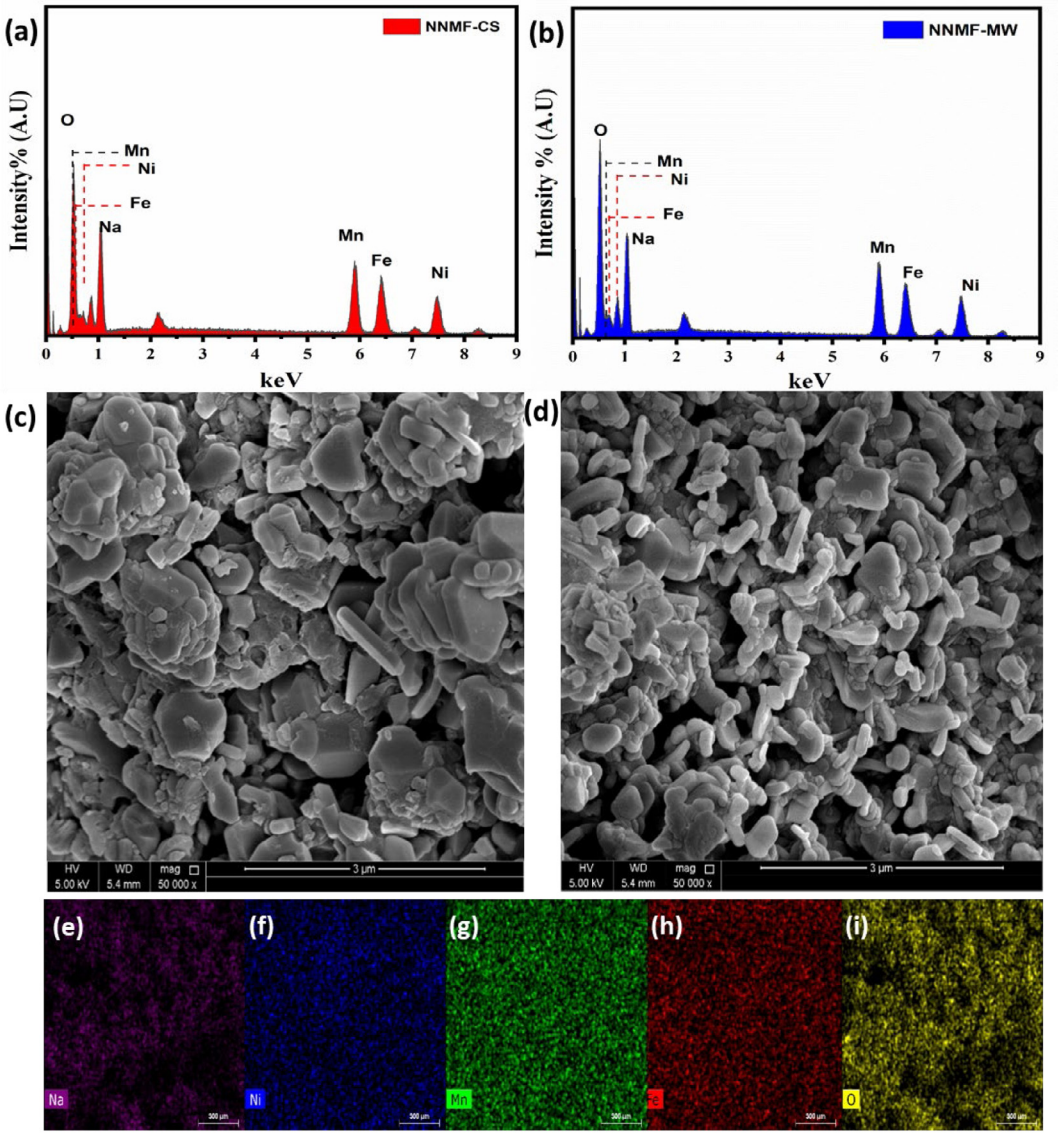

Fig. 3. Elemental dispersive X-ray analysis of (a) NNMF-CS and (b) NNMF-MW materials and their SEM Images (magnification scale 3 µm) (c) and (d). Elemental mapping images (e-i) (magnification scale 300 µm) .

0.2-0.4 µm size agglomerating to generate secondary larger particles of 0.4–0.7 µm size. Although the morphology is not uniform, this primary and agglomerated secondary arrangement can be observed throughout the material (Wang et al., 2016).

Fig. 3(d) shows SEM images of NNM-MW that differ from conventional in that the size of the slab-like layered structure is a comparatively smaller scale with soft edges and tiny particles agglomerated around. It can be viewed as smaller slab particles with sizes ranging from 0.06-0.2 µm agglomerating to generate secondary larger particles ranging from 0.2-0.7 µm.

High-resolution TEM characterized the crystal structures NNMF-CS and NNMF-MW (Wang et al., 2018). HR(high-resolution) TEM images show polycrystalline structure by well aligned circular coordinations of hkl planes. The interplanar spacing of 0.1627 nm in Fig. 4(a) can be attributed to the (202) plane of NNMF-CS. In contrast, the lattice spacing of 0.9218 nm in Fig. 4(b) can be credited to the (202) plane of NNMF-MW, indicating that the interplanar spacing of the (202) plane increases through microwave synthesis. The Selected area electron diffraction (SAED) images shows the polycrystalline nature of the NNMF-CS and NNMF-MW materials by the concentric ring-like structure. In comparison, more prominent ring-crystal structures in Fig. 4(f) for NNMF-MW material is formed than the NNMF-CS material in Fig. 4(e). The TEM images in Fig. 4(e) demonstrate that each primary particle is around 250 nm in size for NNMF-CS and in Fig. 4(f) 60 nm in size for NNMF-MW, which corresponds to the SEM image sizes. The lattice fringes exist in numerous directions, as shown in Fig. 4(a) and (b), indicating the material's polycrystalline character.

The Density functional theory (DFT) calculation can be used to explain some of the properties to further understand the origin of improved air stability kinetics of the NNMF-CS and NNMF-MW materials. DFT simulations were performed to study the influence of Na^+ vacancies on the intrinsic electronic structure and Na^+ diffusion energy barriers to better understand the basis of increased air stability and kinetics of the NNMF cathode. All the density functional theory calculations were performed with the pseudopotential plane wave approach implemented in the VASP (Vienna Ab-initio Simulation Package) (Phys. Rev. B 54, 11169 (1996); Comput. Mater. Sci. 1996, 6, 15), using the plane-wave cutoff energy of 550 eV and the Grimme method (S. Grimme, J. Antony, S. Ehrlich, H. Krieg, J. Chem. Phys.2010, 132, 154104.)

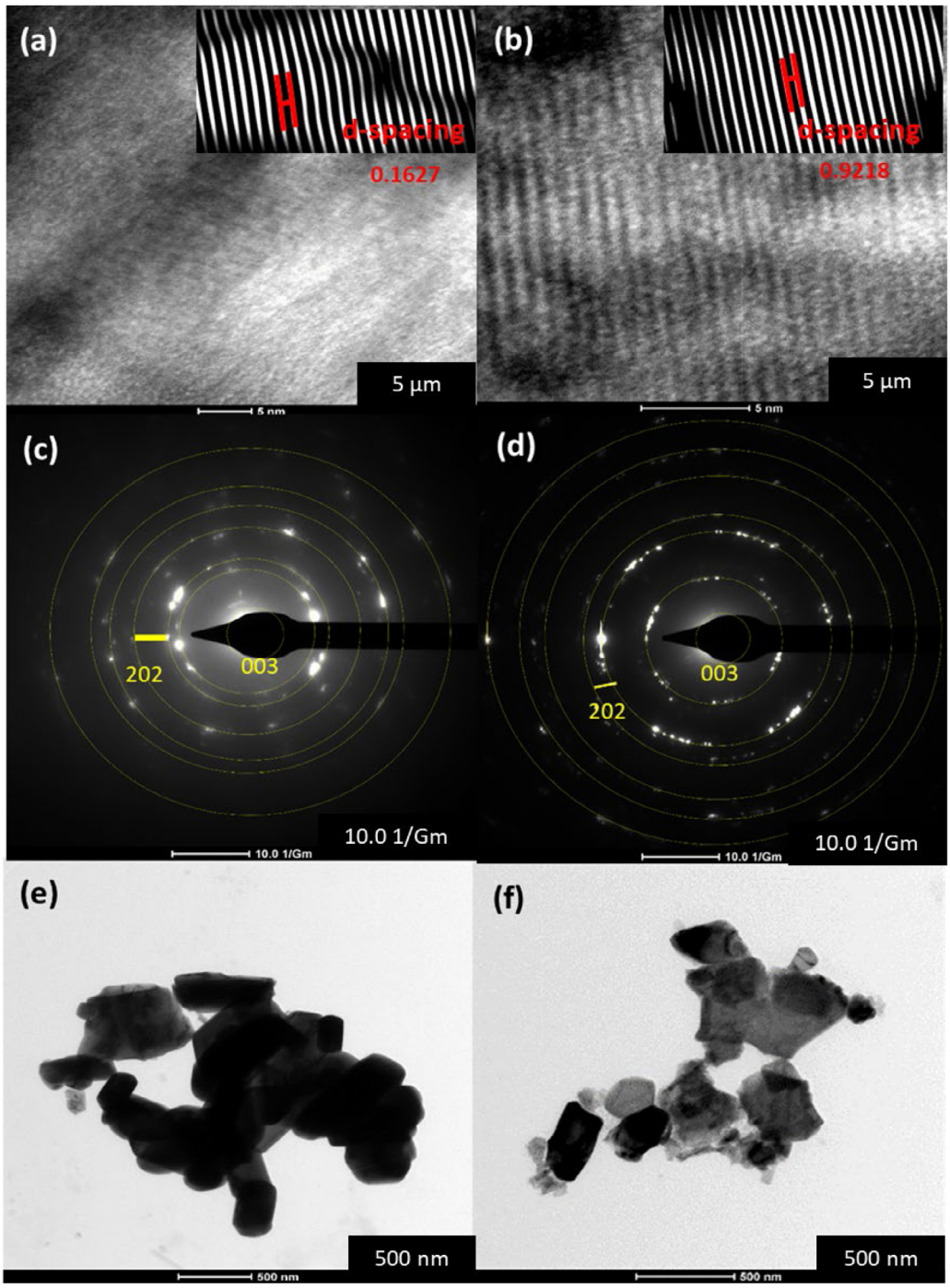

Fig. 4. HRTEM showing lattice spacings (a)(b), d-spacing calculation from HRTEM images (c)(d), elemental and TEM images of NNMF-CS (right column) and NNMF-MW (left column).

for the van der Waals correction. The Perdew–Burke–Ernzerhof generalized gradient approximation was engaged for the geometry optimization until the Feynman forces on each atom dropped below 0.001 eVÅ^{-1}. The k-meshes 6 × 6 × 3 and 9 × 9 × 6 were used for the self-consistent and non-self-consistent calculations, respectively.

Fig. 7 presents the NNMF computation model. $MnNiFeO_4$ contains a layered structure and crystallizes in the trigonal $R\bar{3}$ m space group. The optimized lattice constants turn out to be 2.84 Åand 27.01 Å. The bond lengths are 1.91 Å(Mn–O), 1.88 Å(Ni–O), and 1.90 Å(Fe–O). The crystal symmetry remains intact with Na intercalation to produce $NaMnNiFeO_2$, so each Na^{1+} sits between the two MO_2 (M = Mn, Ni, Fe) layers constituted of different transition metals and coordinates with six O^{2-} atoms to form NaO_6 octahedra.

The optimized lattice constants are 3.06 Åand 32.17 Å. The bond lengths are 2.06 Å(Mn–O and Ni–O) and 2.05 Å(Fe–O)(see Fig. 5).

From the density of states calculations, $MnNiFeO_4$ is a half-metallic material (band gap in the spin-up channel, whereas a metallic behavior in the spin-down channel), and $NaMnNiFeO_2$ is a metallic material. Smaller ionic radii of Mn^{3+}(0.65 Å) as

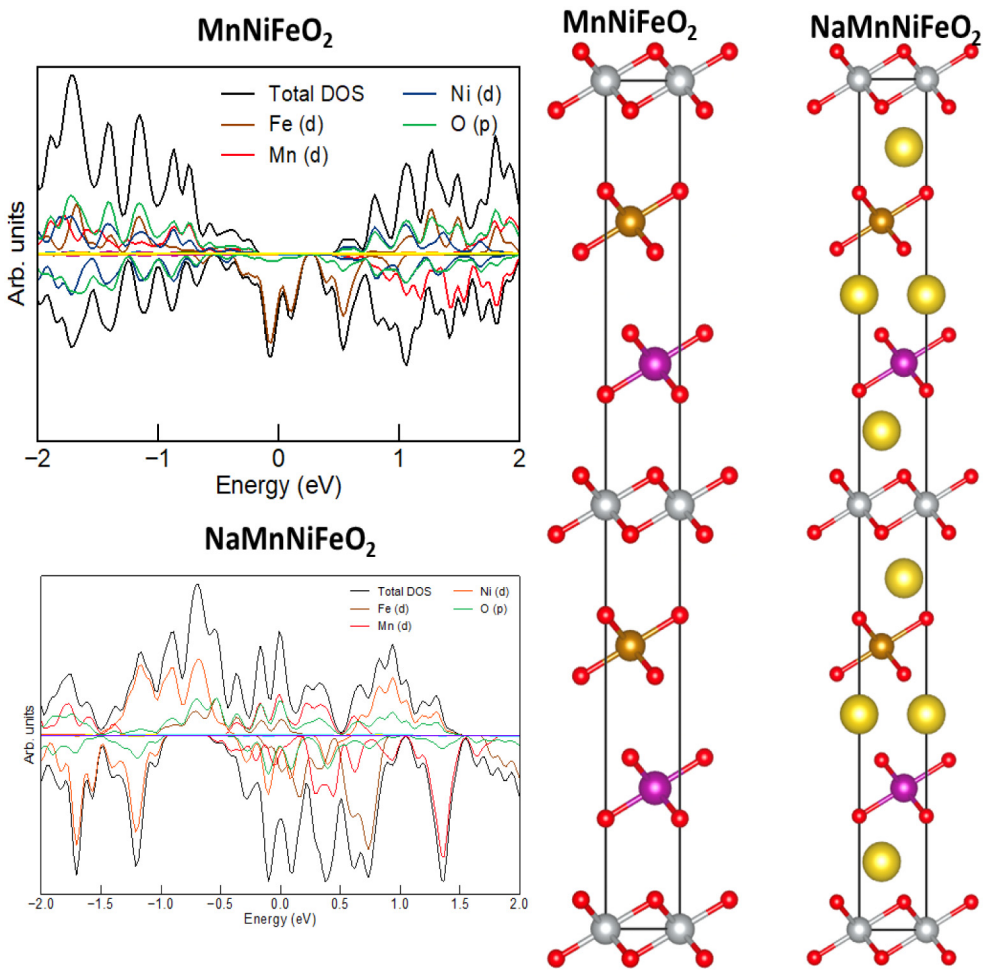

Fig. 5. Computational model for Na^+ ion intercalation and de intercalation process of NNMF material.

compared to Mn^{2+}(0.82 Å) cause the lattice parameter (a) to decrease (Wang et al., 2015).

Only a minority of molecules are triggered when the temperature rises under conventional conditions. The temperature on the reaction vessel's surface is always higher than the internal temperature, and thermal conduction delivers heat energy to the reaction mixture. Energy is given to the reaction mixture by thermal conduction. Microwave radiation, on the other hand, is directly transported to reactant species in MW-assisted processes. The reaction mixture absorbs microwave radiation, resulting in superheating and the production of activation of bulk molecules (Pfeiffer et al., 2022; Vijayalakshmi and Sivaraj, 2015). As a result, the sodium-ion intercalation route is far more practicable than the conventional route.

Initial weight loss can be noticed in the TGA-DSC experiment between 80–150 °C, accompanied by an endothermic reaction, and the creation of water illustrates a approximately 0.35% reduction in the material's original weight for both NNMF-CS material in red and NNMF-MW material in blue as shown in Fig. 6(a). In the DSC measurement, a second endothermal signal is found with a reaction initiation of 250 °C. Water and carbon dioxide are formed as a result of this process. Whereas water evolution peaks at 300 °C and continues until 420 °C, carbon dioxide evolution continues until 800 °C (Pfeiffer et al., 2022). Overall mass loss after reaching 800 °C accounted for 8.28% and 4.82% for NNMF-CS and NNMF-MW materials, respectively, as shown in Fig. 6(a) and (b).

A Fourier transform infrared spectroscopy confirms the presence of Fe and Mn in the material (FTIR). Fig. 7(a) illustrates the FTIR spectrum of the microwave-sintered NNFMO material and NNMF-CS material. The analysis is performed for wavelengths ranging from 500 to 4000 cm^{-1}. Peaks between 400 and 600 are indicative of Fe-O bonding (Fang et al., 2017). The characteristic peak at 600 cm^{-1}, in particular, is attributed to the stretching vibration mode of Fe-O (Durai and Badhulika, 2020; Yuan et al., 2015). The intrinsic stretching vibration of the metal-oxygen band at 556 cm^{-1} (Demir et al., 2013) indicates the intrinsic stretching vibration of metal at the tetrahedral site.

The significant peak at 882 is caused by CO_3^{2-} (Prekajski et al., 2016), which could be attributed to the citric acid utilized in the production stage. However, two visible spectral bands at 1119 and 1689 cm^{-1} are attributed to carbon (C) stretching vibrations caused by residual citric acid. Because of inter-atomic vibrations, metal oxide generally predicts peaks below 1000 cm^{-1}. The Na-O bond is responsible for the absorption peak at 1429 cm^{-1}. In Fig. 7(a), the broad absorptions at 2860 and 3474 cm^{-1} can be attributed to the O-H stretching mode and H-O-H bending mode from interstitial waters. Furthermore, the significant broad adsorption of the O-H vibration peak by NNMF-MW compared to NNMF-CS indicates that the material's hydrophobicity has changed (Rahmawati et al., 2020; Rami Reddy et al., 2015; Kouthaman et al., 2020).

The Raman spectra of NNMF-CS and NNMF-MW, as shown in Fig. 7(b), exhibit a tiny peak at 110 cm^{-1} that corresponds to the Na^+ translation mode of vibration against the octahedron, as the octahedron has six vibrational modes within the hexagonal structure where octahedral gaps exist between the two lattice layers.

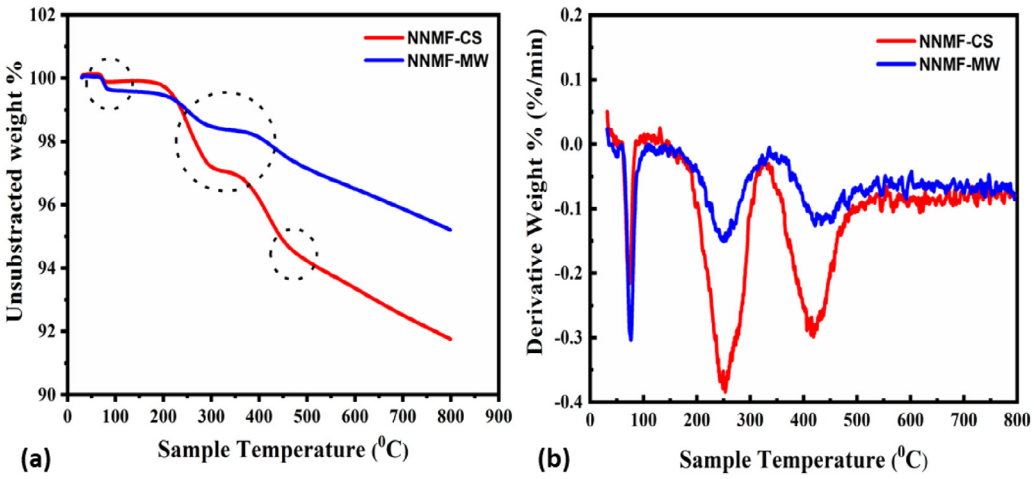

Fig. 6. (a) Comparison of TGA analysis and (b) DSC analysis of NNMF-CS and NNMF-MW materials.

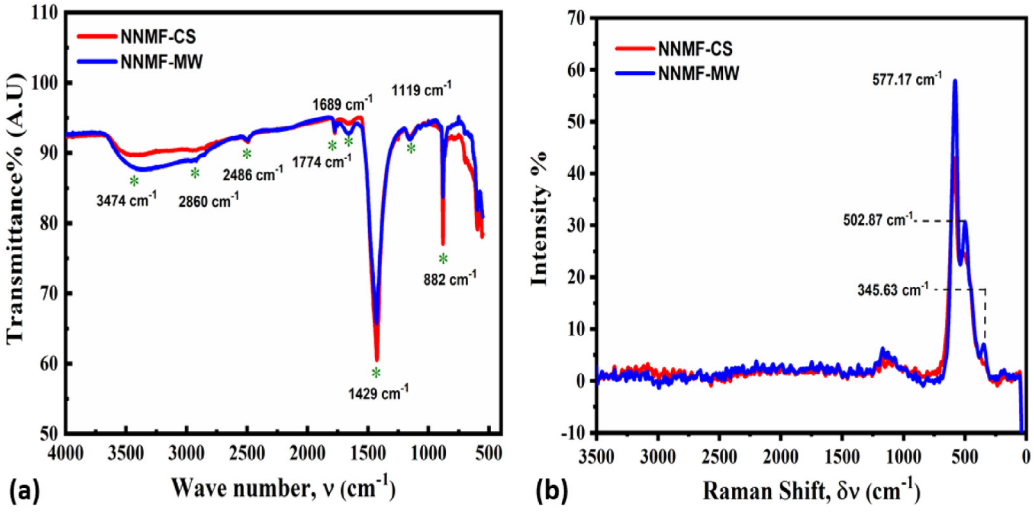

Fig. 7. Comparative analysis of (a) FT-IR and (b) Raman Shift of NNMF-CS and NNMF-MW materials.

The bands detected at 500 cm^{-1} and 600 cm^{-1} correspond to the T_{2g}, $\nu_2(E_g)$, and A_{1g} modes of vibration, respectively. The band region above 750 cm^{-1} can be attributed to the centrosymmetric space group, which is attributed to the combination ν_1+ ν_5 with F_{2g} (Durai and Badhulika, 2020; Rahmawati et al., 2020).

To compare the microwave sintered and conventional sintered from an electrochemical point of view, various galvanostatic and potentiostatic analysis methods were carried out. The galvanostatic charge–discharge (GCD) curve for the material for the 1st cycle is shown in Fig. 8(a). The GCD analysis was carried out between 2.0 to 4.0 V. The specific discharge capacity obtained from the microwave-sintered material NNFM-MW is higher than the conventional sample. This could be attributed to a higher diffusivity and higher electrical conductivity in the material brought about by the reduced particle size described by the SEM and TEM images. A similar increase in the specific discharge capacity was seen in the work by Nisar et al. (2021), where in it was seen that microwave sintering of the $LiNi_{0.5}Mn_{0.5}O_4$ cathode material resulted in higher specific discharge capacity than the conventional sintered one. Fig. 8(b) presents the cyclability curve of the two materials for 30 cycles. The capacity fading is more fairly distributed over the period for the microwave-sintered material. The conventional sintered material shows dips and highs for the period. As the cycling progresses, the charge–discharge curves Figs. 8(c) and 8(d) indicate that the material's behavior is more uniform and balanced in the microwave sintered material. This might be due to the superior structural stability of the microwave-sintered material to the conventionally sintered material. More equally dispersed cycle data is obtained in the microwave-sintered NNFM- MW, which has higher values of specific discharge capacity than the NNMF-CS material.

The cyclic voltammetry (CV) curves for the NNFM-CS and NNFM-MW for the first cycle are shown in Figs. 9(a) and 9(d), while the CV curves for cycle changes are shown in Fig. 9(b) and Fig. 9(d) for the NNFM-CS and NNFM-MW material respectively. The broad CV curve indicates a pseudo-capacitive behavior with the electrical double layer getting formed at the electrode–electrolyte interface. The peaks present, on the other hand, represents the faradaic processes. The cathodic peak (oxidation peak) in the CV diagram of the NNFM-CS is at 3.32 V, and the anodic peak (reduction peak) is at 2.79 V as Fig. 9(a). This is from the Ni^{2+}/Ni^{3+} redox pair, and the other redox pairs of Mn^{2+}/Mn^{3+} and Fe^{3+}/Fe^{4+} peaks are not distinct. The difference between the cathodic and anodic peaks is high and comes to a value of 530 mV (3.32-2.79V). This indicates it does not belong to the perfectly reversible electrochemical reaction (Elgrishi et al., 2018), but in the case of NNFM-MW, the differences between the peaks are reduced to a value of 240 mV; this indicates the material synthesized by microwave sintering provides enhances structural reversibility than the conventional sintered material.

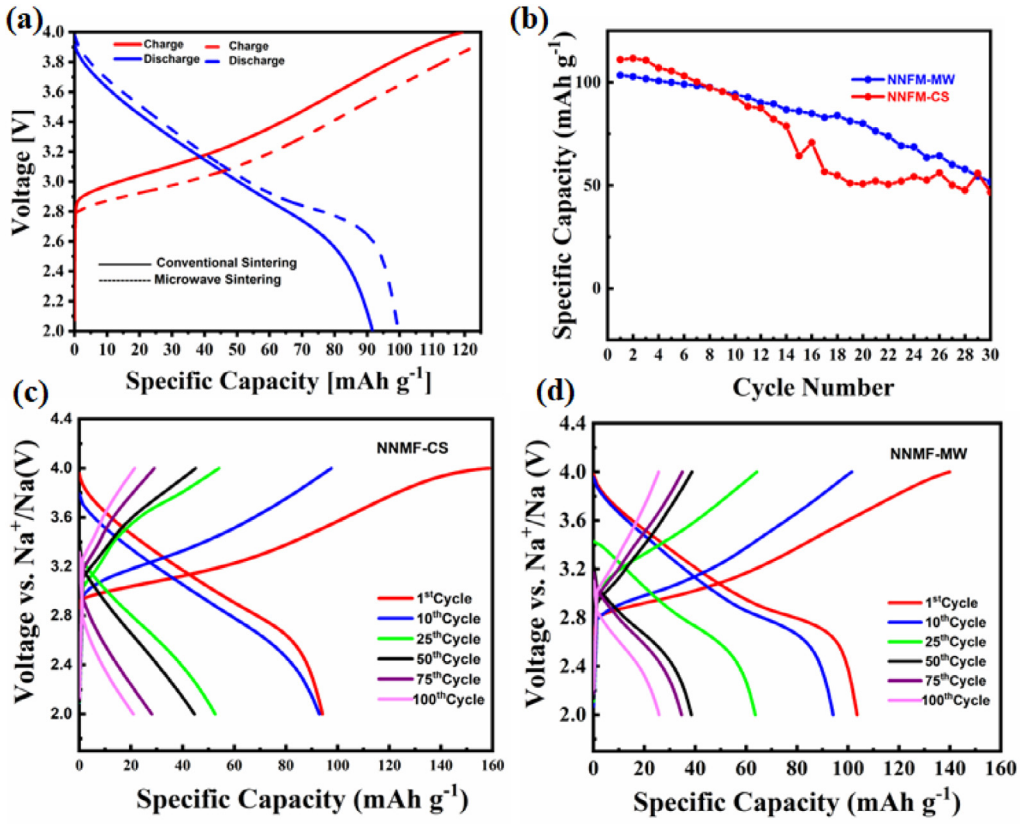

Fig. 8. (a) The charge discharge curve of the NNMF-CS and NNMF-MW materials (b) The capacity retention curve for the NNMF-CS in red and NNMF-MW in blue. The charge–discharge curve at various cycles for the (c) NNMF-CS and (d) NNMF-MW.

This indicates that the electron transfer kinetics is improved due to the reduced size morphology brought about by microwave sintering (Vijayalakshmi and Sivaraj, 2015). According to Fig. 9(c), the anodic redox peak at 3.08 V and the reduction peak at 2.814 V indicate the Ni^{2+}/Ni^{3+} redox pair (Li et al., 2020). A peak is visible at 3.6 V, which is from the Mn^{2+}/Mn^{3+} (Nisar et al., 2018). The shift in the anodic current peak is visible in both systems upon cycling. It could be attributed to the surface electrolyte interface (SEI) formed at the anode, further limiting the easy transfer of electrons between the cathode and anode.

A sequence of current pulses followed by a relaxation period during which no current flows through the cell compensates GITT method. The equilibrium profile produced by galvanostatic intermittent titration (GITT) measurements was conducted at a 1/10C rate during the first cycle to improve the comprehension of the electrochemical reactions occurring in the NNMF-CS and NNMF-MW, as shown in Fig. 10. GITT elucidates the mechanisms of sodium diffusion in the material. The overpotential affects sodium diffusion; the higher the overpotential, the slower the diffusion of active species. The inclined voltage plateau indicates a single-phase operation. Fig. 10(a and b) show negligible over potential until 3.1 V during charging. Fig. 10(a) shows more sluggish sodium diffusion in the initial applied voltage (2.75V) and smooth intercalating related to redox peaks on further increased applied voltage, whereas Fig. 10(b) shows comparatively smooth sodium intercalation and deintercalation.

Fig. 10(a), on the other hand, demonstrates that in the case of NNMF-CS, the continuous sodium diffusion till 4.0 V, with a spikes curve, can be coupled with considerable polarization and 75% sodium extraction during the process. A smooth upward trend is seen for NNMF-MW until 85% of the sodium is removed, resulting in significantly lower polarization Fig. 10(b). This implies that the NNMF-CS and NNMF-MW materials are electrochemically more active, that the NNMF-MW material has improved considerably with synthesis. The findings of the electrochemical profiles accord with the results of the incremental capacity curves in Fig. 8.

During charging, the current is positive, and when discharging, it is negative. Incorporating the GITT curve, it is possible to determine the sodium-ion diffusion coefficient to comprehend the sodium kinetics process. The fluctuation of the chemical diffusion coefficient of Na-ions (D^{+}_{Na}), as derived from the GITT profiles in NNMF-CS and NNMF-MW, is depicted in the supplemental information figure. The Na-ion diffusion coefficients exhibit a similar downward pattern during discharge and a similar upward trend during charging. An alteration in the amount of sodium in the crystal structure likely causes this fluctuation in sodium ion diffusion during the cycle process. The D^{+}_{Na} in NNMF-CS exhibits 2×10^{-3}–$4 \times 10^{-3}\,m^2\,s^{-1}$, which is remarkably lower than the corresponding Na diffusivity in MMNF-MW (1×10^{9}–$3.58 \times 10^{9}\,m^2\,s^{-1}$). Indirectly supporting multiple-vacancy Na-ion diffusion in the NNMF-MW, the calculation results and the GITT measurement show that Na-ion diffusion in the NNMF-MW is faster than that in the NNMF-CS.

One of the most effective approaches for retrieving insights on the diffusion coefficient of the electrode's active materials is the potentiostatic intermittent titration technique (PITT), along with the galvanostatic intermittent titration technique (GITT). The series of 0.02 V pulses from the starting battery voltage to 4.0 V can be seen, as well as the subsequent relaxation step in which the potential falls. In contrast, the potential marginally rises with each pulse of −0.02 V potential during discharge. The relative voltage-current behavior during the PITT experiment is also shown in Figures S4 and S5 (supporting information) and provides a better representation of this pattern by plotting the generated current and the potential at the 4.0 V upper limit

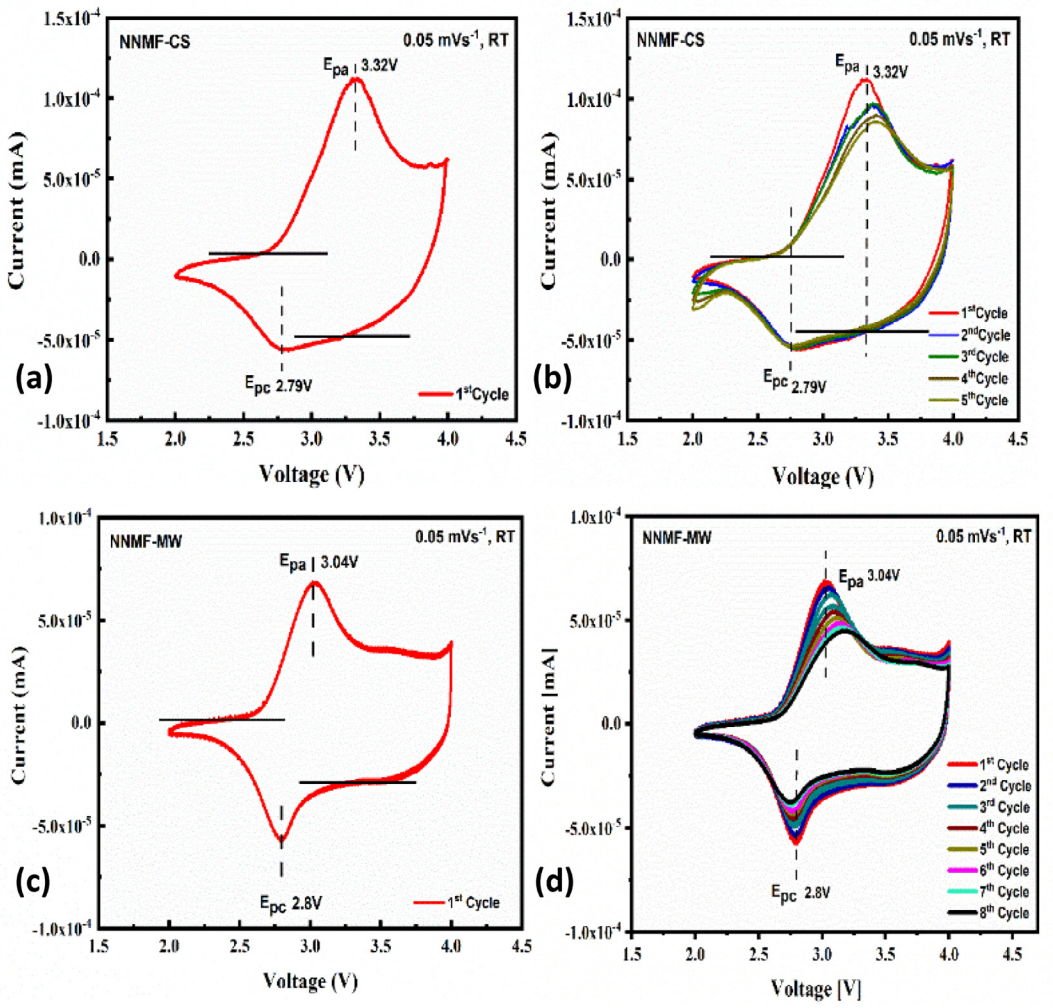

Fig. 9. Cyclic voltammetry curve for the (a) first cycle of conventional sintered NaNi $_{0.33}Fe_{0.33}Mn_{0.33}O_2$(b) for the first 5 cycles of the conventional sintered NaNi $_{0.33}Fe_{0.33}Mn_{0.33}O_{2(c)}$ first cycle of the microwave sintered NaNi $_{0.33}Fe_{0.33}Mn_{0.33}O_2$(d) for the first 8 cycles of the microwave sintered NaNi $_{0.33}Fe_{0.33}Mn_{0.33}O_2$.

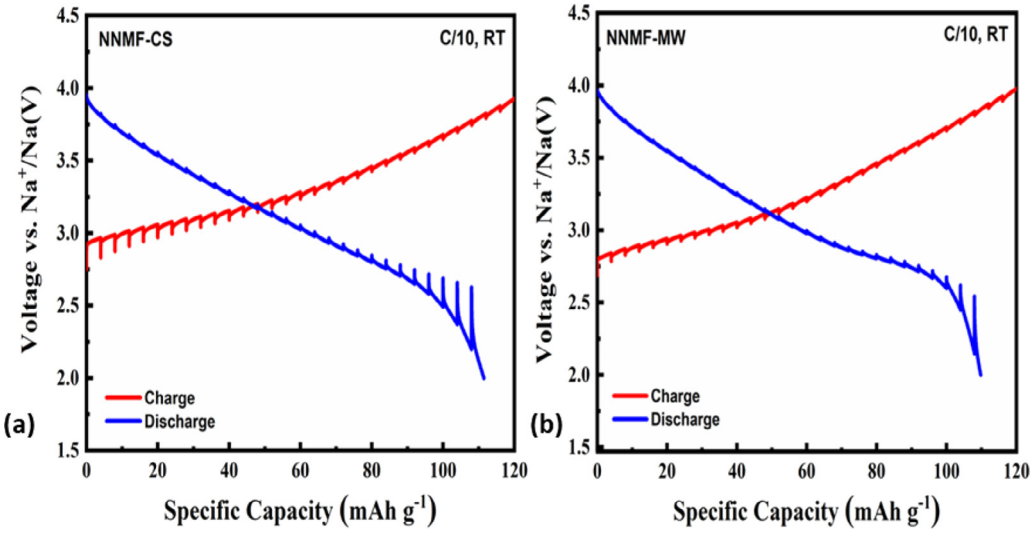

Fig. 10. GITT analysis at 1C for (a) NNMF-CS and (b) NNMF-MW cathode materials.

against time. Figures S4 and S5 show the potential signal and the logarithm of the current against time. In a single-phase region, the current declined exponentially with time during each potential step. The diffusion coefficient D_{Na}^{+} for each potential pulse can be estimated from this plot. Comprehending the diffusion kinetics and computing the diffusion coefficient (supplementary information) was necessary. In comparison MMNF-MW exhibits Na ion diffusivity (1.1 x10^{-3}–6.9 × 10^{-4} m^2 s^{-1}), to the charging and

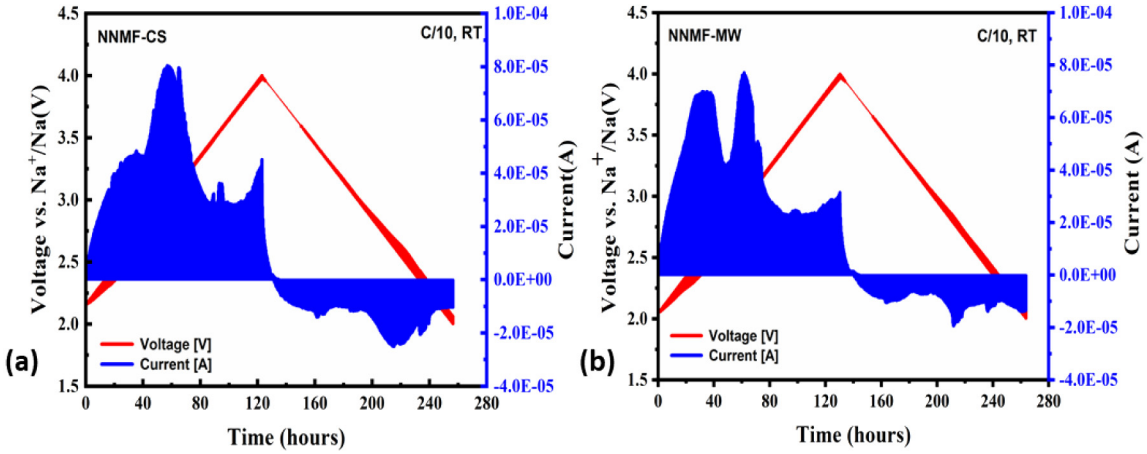

Fig. 11. Potential (red line) and current (blue line) vs. time resulting from the PITT experiment for (a) NNMF-CS and (b) NNMF-MW materials.. (For interpretation of the references to color in this figure legend, the reader is referred to the web version of this article.)

discharging of NNMF-CS demonstrate (1.6×10^{-3}—1.1×10^{-3} m^2s^{-1}) in Fig. 10 and Fig. 11(a) and (b).

During this time, the current exponential decreases (Cottrel-type). The multicomponent NNMF sample's current curves from the PITT measurement exhibit a Cottrel-type law, which is a sign of a solid solution insertion process.

EIS measurements were taken during the first 40 cycles at a 1C rate during the charging and discharging stages which are quite reasonable to study the formation of SEI layer and its impact on the electrochemical performance of the cycled cathode materials. The corresponding Nyquist plot obtained by EIS analysis is shown in Fig. 12. In the Nyquist plot, the symbol+line curve represents the experimental data points, and the NNMF-MW sample's fitted data are shown as continuous black lines. The obtained data were fitted to an electrical equivalent circuit consisting of capacitances, constant phase elements (CPE_1 and CPE_2), and the finite Warburg impedance; the circuit is shown in supplementary info Figure S6(b). R_e represents the electrolyte resistance or the bulk resistance; charge transfer resistance R_{ct} is given by the R_2&R_3, which represents the electrode/electrolyte interface. For fitting experimental data inside the frequencies regime, RelaxIS-3 software was employed.

From the EIS plots, it can be inferred that the bulk resistance remains constant throughout all the cycles. It indicates the stable ionic resistivity of the employed electrolyte. The value is found to be 58.80 Ω. The next semicircle represents the resistance formed due to the formation of the SEI layer. The semicircle is increasing in size, representing the increased resistance developing from the SEI layer. This happens as cycling progresses; the SEI layer becomes thick upon covering more cycles and increases the resistance hindering easier intercalation/deintercalation of Na+ into/from the host structure. Its value is found to be 768.86 Ω after the 1st cycle, 924.33 Ω after the 10th cycle, 1018 Ω after the 20th cycle, 1658.69 Ω after the 30th cycle, 1510.01 Ω after the 40th cycle, 1511.32 Ω after 50th cycle. The straight Warburg impedance curve clearly represents the single-phase reaction in the first cycle in the EIS plot. After the first cycle, this is found to be slightly changing as the cycle progresses. This is also observed in the GCD, where the capacity is found to be fading for consecutive cycles, indicating higher resistance.

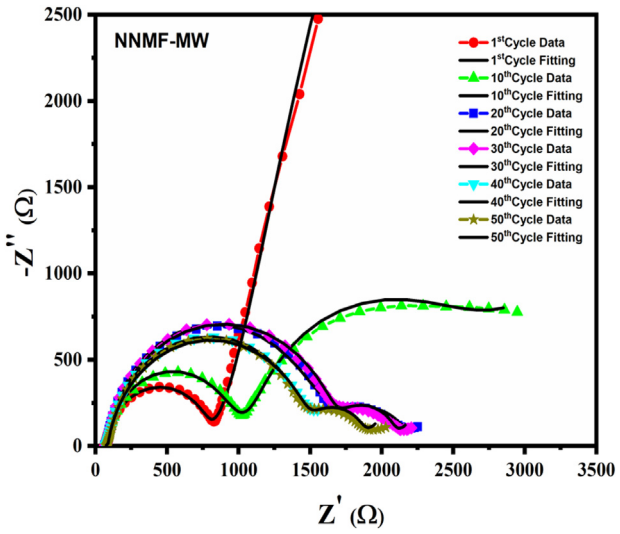

Fig. 12. EIS (Nyquist plot) spectra of the NNMF-MW sodium conversion system at different states of charge/discharge. (Equivalent circuit diagram Supplementary Information figure S6:(b)).

4. Conclusion

- $Na_1Ni_{0.33}Mn_{0.33}Fe_{0.33}O_2$-(NNMF) was developed through a facile microwave-assisted sol–gel technique and its structural, thermal and electrochemical properties were compared with the same synthesized conventional solid-state synthesis route.
- A remarkable reduction in the sintering process time is noticed in the microwave-assisted sol–gel synthesis technique when compared to the conventional solid-state synthesis route confirming its decent cost-effectiveness.
- $Na_1Ni_{0.33}Mn_{0.33}Fe_{0.33}O_2$ developed through the microwave-assisted sol–gel synthesis technique demonstrates improved thermal stability as compared to the conventionally sintered technique.
- The electrochemical performance of $Na_1Ni_{0.33}Mn_{0.33}Fe_{0.33}O_2$ developed through the microwave-assisted sol–gel synthesis technique is comparable to the same cathode material produced through the conventional sintering process.
- EIS analysis confirms that the capacity fading of $Na_1Ni_{0.33}Mn_{0.33}Fe_{0.33}O_2$ materials during cycling essentially due to the formation of SEI layer and its gradual thickening, upon cycling which hinders the efficient movement of Na+ into/from the host structure.
- Intercalation/deinterclation of Na+ into/from $Na_1Ni_{0.33}Mn_{0.33}Fe_{0.33}O_2$ is occurred through a single phase reaction regardless of the synthesis route rather than a biphasic reaction.

- High phase purity, good crystallinity, improved thermal stability, comparable electrochemical performance, and cost-effectiveness of the $Na_1Ni_{0.33}Mn_{0.33}Fe_{0.33}O_2$ developed by microwave-assisted sol–gel method make it attractive for commercial applications. Moreover, the proposed synthesis route can also be applied to other families of cathode materials to develop at a competitive cost.

Declaration of competing interest

The authors declare that they have no known competing financial interests or personal relationships that could have appeared to influence the work reported in this paper.

Data availability

Data will be made available on request.

Acknowledgments

This work was supported by the Qatar National Research Fund (QNRF) grant number NPRP11S-1225-170128. The Central Laboratory Unit (CLU), Qatar University, 2713, Doha, Qatar, provided the microstructural analysis (FE-SEM/EDX and HR-TEM), which the authors would also like to recognize. The writers are entirely responsible for the statements stated herein. Moreover, the authors would also like to thank Zawar Alam Qureshi for his technical assistance with various electrochemical characterizations and pictorial illustration credits to Tasneem Elmakki.

Appendix A. Supplementary data

Supplementary material related to this article can be found online at https://doi.org/10.1016/j.egyr.2023.07.038.

References

Berthelot, R., Carlier, D., Delmas, C., 2011. Electrochemical investigation of the P2-NaxCoO2 phase diagram. Nat. Mater. 10 (1), 74–80. http://dx.doi.org/10.1038/nmat2920.

Bomio, M.R.D., Lavela, P., Santiago, A.A.G., Motta, F.V., Tirado, J.L., 2022. Optimized synthesis of Na2/3Ni1/3Mn2/3O2 as cathode for sodium-ion batteries by rapid microwave calcination. Ceram. Int. http://dx.doi.org/10.1016/j.ceramint.2022.12.105.

Bomio, M., Lavela, P., Tranquilin, R.L., da Motta, F.V., Tirado, J.L., 2023. Microwave calcination as a novel route to prepare high performance Mg-doped Na2/3Ni1/3Mn2/3O2 cathodes for sodium-ion batteries. J. Electroanal. Soc. 930, 117157. http://dx.doi.org/10.1016/j.jelechem.2023.117157.

Burova, D., et al., 2019. The rapid microwave-assisted hydrothermal synthesis of NASICON-structured Na3V2O2: X(PO4)2F3-2 x ($0 < x \leq 1$) cathode materials for Na-ion batteries. RSC Adv. 9 (34), 19429–19440. http://dx.doi.org/10.1039/c9ra02257k.

Carlier, D., et al., 2011. The P2-Na2/3Co2/3Mn1/3O2 phase: Structure, physical properties and electrochemical behavior as positive electrode in sodium battery. J. Chem. Soc. Dalton Trans. 40 (36), 9306–9312. http://dx.doi.org/10.1039/c1dt10798d.

Chayambuka, K., et al., 2020. From Li-ion batteries toward Na-ion chemistries: Challenges and opportunities. http://dx.doi.org/10.1002/aenm.202001310.

Demir, A., Topkaya, R., Baykal, A., 2013. Green synthesis of superparamagnetic Fe3O4 nanoparticles with maltose: Its magnetic investigation. Polyhedron 65, 282–287. http://dx.doi.org/10.1016/j.poly.2013.08.041.

Ding, J.J., Zhou, Y.N., Sun, Q., Yu, X.Q., Yang, X.Q., Fu, Z.W., 2013. Electrochemical properties of P2-phase Na0.74CoO2 compounds as cathode material for rechargeable sodium-ion batteries. Electrochim. Acta 87, 388–393. http://dx.doi.org/10.1016/j.electacta.2012.09.058.

Diouf, B., Pode, R., 2015. Potential of lithium-ion batteries in renewable energy. Renew. Energy 76, 375–380. http://dx.doi.org/10.1016/j.renene.2014.11.058.

Durai, L., Badhulika, S., 2020. Facile synthesis of large area pebble-like β-NaFeO2 perovskite for simultaneous sensing of dopamine, uric acid, xanthine and hypoxanthine in human blood. Mater. Sci. Eng. C 109 (2019), 110631. http://dx.doi.org/10.1016/j.msec.2020.110631.

Elgrishi, N., Rountree, K.J., McCarthy, B.D., Rountree, E.S., Eisenhart, T.T., Dempsey, J.L., 2018. A practical beginner's guide to cyclic voltammetry. J. Chem. Educ. 95 (2), 197–206. http://dx.doi.org/10.1021/acs.jchemed.7b00361.

Fang, N., et al., 2017. Synthesis and adsorption properties of [Cu(L)2(H2O)]H2[Cu(L)2(P2Mo5O23)]· 4H2O/Fe3O4 nanocomposites. RSC Adv. 7 (41), 25325–25333. http://dx.doi.org/10.1039/c7ra02133kj.

Ge, P., Fouletier, M., 1988. Electrochemical intercalation of sodium in graphite. Solid State Ion. 28–30 (PART 2), 1172–1175. http://dx.doi.org/10.1016/0167-2738(88)90351-7.

Goodenough, J.B., Kim, Y., 2010. Challenges for rechargeable Li batteries. Chem. Mater. 22 (3), 587–603. http://dx.doi.org/10.1021/cm901452z.

Gür, T.M., 2018. Review of electrical energy storage technologies, materials and systems: challenges and prospects for large-scale grid storage. Energy Environ. Sci. 11 (10), 2696–2767. http://dx.doi.org/10.1039/c8ee01419a.

Hirsh, H.S., Li, Y., Tan, D.H.S., Zhang, M., Zhao, E., Meng, Y.S., 2020. Sodium-ion batteries paving the way for grid energy storage. Adv. Energy Mater. 10 (32), 1–8. http://dx.doi.org/10.1002/aenm.202001274.

Hoseinzadeh, S., Ghasemiasl, R., Bahari, A., Ramezani, A.H., 2017. n-type WO3 semiconductor as a cathode electrochromic material for ECD devices. J. Mater. Sci., Mater. Electron. 28 (19), 14446–14452. http://dx.doi.org/10.1007/s10854-017-7306-7.

Kalluri, S., 2016. Nano-engineering and advanced characterizations of layered-structure electrode materials for lithium-ion and sodium-ion batteries, Doctor of Philosophy thesis. School of Mechanical, Materials and Mechatronics Engineering, University of Wollongong, https://ro.uow.edu.au/theses/4734.

Kebede, M.A., Yannopoulos, S.N., Sygellou, L., Ozoemena, K.I., 2017. High-voltage LiNi 0.5 Mn 1.5 O 4- δ spinel material synthesized by microwave-assisted thermo-polymerization: Some insights into the microwave-enhancing physico-chemistry. J. Electrochem. Soc. 164 (13), A3259–A3265. http://dx.doi.org/10.1149/2.1471713jes.

Kim, D., Lee, E., Slater, M., Lu, W., Rood, S., Johnson, C.S., 2012. Layered Na[Ni 1/3Fe 1/3Mn 1/3]O 2 cathodes for Na-ion battery application. Electrochem. Commun. 18 (1), 66–69. http://dx.doi.org/10.1016/j.elecom.2012.02.020.

Komaba, S., Takei, C., Nakayama, T., Ogata, A., Yabuuchi, N., 2010. Electrochemical intercalation activity of layered NaCrO2 vs LiCrO2. Electrochem. Commun. 12 (3), 355–358. http://dx.doi.org/10.1016/j.elecom.2009.12.033.

Komaba, S., Yabuuchi, N., Nakayama, T., Ogata, A., Ishikawa, T., Nakai, I., 2012. Study on the reversible electrode reaction of Na 1−xNi 0.5Mn 0.5O 2 for a rechargeable sodium-ion battery. Inorg. Chem. 51 (11), 6211–6220. http://dx.doi.org/10.1021/ic300357d.

Kouthaman, M., Kannan, K., Arjunan, P., Meenatchi, T., Subadevi, R., Sivakumar, M., 2020. Novel layered O3-NaFe0.45Co0.45Ti0.1O2 cathode material for sodium batteries. Mater. Lett. 276, 128181. http://dx.doi.org/10.1016/j.matlet.2020.128181.

Kubota, K., Yabuuchi, N., Yoshida, H., Dahbi, M., Komaba, S., 2014. Layered oxides as positive electrode materials for Na-ion batteries. MRS Bull. 39 (5), 416–422. http://dx.doi.org/10.1557/mrs.2014.85.

Leurent, H., 2023. Consumers are key to tackling the global crises – let's work with them. In: World Economic Forum.

Li, N., et al., 2020. A comprehensive study of the multiple effects of Y/Al substitution on O3-type NaNi0.33Mn0.33Fe0.33O2 with improved cycling stability and rate capability for Na-ion battery applications. Nanoscale 12 (32), 16831–16839. http://dx.doi.org/10.1039/d0nr04262e.

Liu, X.Y., Wang, K.X., Chen, J.S., 2016. Template-directed metal oxides for electrochemical energy storage. Energy Storage Mater. 3, 1–17. http://dx.doi.org/10.1016/J.ENSM.2015.12.002.

Lu, Z., MacNeil, D.D., Dahn, J.R., 2001. Layered cathode materials Li[NixLi(1/3-2x/3)Mn(2/3-x/3)]O2 for lithium-ion batteries. Electrochem. Solid-State Lett. 4 (11), A191. http://dx.doi.org/10.1149/1.1407994/XML.

Ma, X., Chen, H., Ceder, G., 2011. Electrochemical properties of monoclinic NaMnO2. J. Electrochem. Soc. 158 (12), A1307. http://dx.doi.org/10.1149/2.035112jes.

Mizushima, K., Jones, P.C., Wiseman, P.J., Goodenough, J.B., 1980. LixCoO2 (0<x<-1): A new cathode material for batteries of high energy density. Mater. Res. Bull. 15 (6), 783–789. http://dx.doi.org/10.1016/0025-5408(80)90012-4.

Mohanty, H.S., Kumar, A., Sahoo, B., Kurliya, P.K., Pradhan, D.K., 2018. Impedance spectroscopic study on microwave sintered (1 − x) na0.5bi0.5tio3–x BaTiO3 ceramics. J. Mater. Sci., Mater. Electron. 29 (8), 6966–6977. http://dx.doi.org/10.1007/s10854-018-8683-2.

Mortemard de Boisse, B., Carlier, D., Guignard, M., Delmas, C., 2013. Structural and electrochemical characterizations of P2 and new O3-Na x Mn 1-y Fe y O 2 phases prepared by auto-combustion synthesis for na-ion batteries. J. Electrochem. Soc. 160 (4), A569–A574. http://dx.doi.org/10.1149/2.032304jes.

Nisar, U., et al., 2018. Sodium intercalation/de-intercalation mechanism in Na4MnV(PO4)3 cathode materials. Electrochim. Acta 292, 98–106. http://dx.doi.org/10.1016/j.electacta.2018.09.111.

Nisar, U., et al., 2021. Fast and scalable synthesis of LiNi 0.5 Mn 1.5 O 4 cathode by sol–gel-assisted microwave sintering. Energy Technol. 9 (7), 2100085. http://dx.doi.org/10.1002/ente.202100085.

Pan, H., Hu, Y.-S., Chen, L., 2013. Room-temperature stationary sodium-ion batteries for large-scale electric energy storage. Energy Environ. Sci. 6 (8), 2338. http://dx.doi.org/10.1039/c3ee40847g.

Paulsen, J.M., Dahn, J.R., 1999. Studies of the layered manganese bronzes, Na [Mn1-x Mx]O2 with M=Co, Ni, Li, and [Mn1-x Mx]O2 prepared by ion-exchange. Solid State Ion. 126, 3–24.

Pfeiffer, L.F., et al., 2022. Layered P2-NaxMn3/4Ni1/4O2 cathode materials for sodium-ion batteries: Synthesis, electrochemistry and influence of ambient storage. Front. Energy Res. 10 (May), 1–17. http://dx.doi.org/10.3389/fenrg.2022.910842.

Prekajski, M., et al., 2016. Ouzo effect-new simple nanoemulsion method for synthesis of strontium hydroxyapatite nanospheres. J. Eur. Ceram. Soc. 36 (5), 1293–1298. http://dx.doi.org/10.1016/j.jeurceramsoc.2015.11.045.

Qureshi, Z.A., Tariq, H.A., Hafiz, H.M., Shakoor, R.A., AlQaradawi, S., Kahraman, R., 2022. Influence of graphene wrapped-cerium oxide coating on spherical LiNi0.5Mn1.5O4 particles as cathode in high-voltage lithium-ion batteries. J. Alloys Compd. 920, http://dx.doi.org/10.1016/j.jallcom.2022.165989.

Rahmawati, F., Kusumaningtyas, A.A., Saraswati, T.E., Prasetyo, A., Suendo, V., 2020. Mn-doped NaFeO2 from a low purity-Fe precursor and its performance as cathode for sodium-ion battery. Inorg. Nano-Metal Chem. 1–8. http://dx.doi.org/10.1080/24701556.2020.1790003.

Rami Reddy, B.V., Ravikumar, R., Nithya, C., Gopukumar, S., 2015. High performance NaxCoO2 as a cathode material for rechargeable sodium batteries. J. Mater. Chem. A Mater. 3 (35), 18059–18063. http://dx.doi.org/10.1039/c5ta03173g.

Sendova-Vassileva, M., Stoyanova, R., Carlier, D., Yoncheva, M., Zhecheva, E., Delmas, C., 2010. Raman spectroscopy study on $Na_{2/3}Mn_{1-x}Fe_xO_2$ oxides. In: 5th Forum on New Materials Part C, Vol. 74, No. May 2014. pp. 60–65. http://dx.doi.org/10.4028/www.scientific.net/ast.74.60.

Suryakala, K., Marikkannu, K.R., Paruthimal Kalaignan, G., Vasudevan, T., 2007. Synthesis and characterization of LiCo x Mn 2-x O 4 powder by a novel CAM microwave-assisted sol–gel method for Li ion battery. J. Solid State Electrochem. 11 (12), 1671–1677. http://dx.doi.org/10.1007/s10008-007-0325-1.

Tanaka, T., Doi, T., Okada, S., Yamaki, J.I., 2009. Effects of salts in methyl difluoroacetate-based electrolytes on their thermal stability in lithium-ion batteries. Fuel Cells 9 (3), 269–272. http://dx.doi.org/10.1002/FUCE.200800085.

Thackeray, M.M., David, W.I.F., Bruce, P.G., Goodenough, J.B., 1983. Lithium insertion into manganese spinels. Mater. Res. Bull. 18 (4), 461–472. http://dx.doi.org/10.1016/0025-5408(83)90138-1.

Thorne, J.S., Dunlap, R.A., Obrovac, M.N., 2014. Investigation of P2-Na 2/3 Mn 1/3 Fe 1/3 Co 1/3 O 2 for Na-ion battery positive electrodes. J. Electrochem. Soc. 161 (14), A2232–A2236. http://dx.doi.org/10.1149/2.0981414jes.

Vijayalakshmi, K., Sivaraj, D., 2015. Enhanced antibacterial activity of Cr doped ZnO nanorods synthesized using microwave processing. RSC Adv. 5 (84), 68461–68469. http://dx.doi.org/10.1039/c5ra13375.

Wang, X., Ding, Y.L., Deng, Y.P., Chen, Z., 2020. Ni-rich/Co-poor layered cathode for automotive Li-ion batteries: Promises and challenges. Adv. Energy Mater. 10 (12), 1–28. http://dx.doi.org/10.1002/aenm.201903864.

Wang, H., Liao, X.-Z., Yang, Y., Yan, X., He, Y.-S., Ma, Z.-F., 2016. Large-scale synthesis of NaNi 1/3 Fe 1/3 Mn 1/3 O 2 as high performance cathode materials for sodium ion batteries. J. Electrochem. Soc. 163 (3), A565–A570. http://dx.doi.org/10.1149/2.0011605jes.

Wang, C.C., Lin, Y.C., Chou, P.H., 2015. Mitigation of layer to spinel conversion of a lithium-rich layered oxide cathode by substitution of Al in a lithium ion battery. RSC Adv. 5 (84), 68919–68928. http://dx.doi.org/10.1039/c5ra11665a.

Wang, X., Liu, G., Iwao, T., Okubo, M., Yamada, A., 2014. Role of ligand-to-metal charge transfer in O3-type NaFeO 2-NaNiO2 solid solution for enhanced electrochemical properties. J. Phys. Chem. C 118 (6), 2970–2976. http://dx.doi.org/10.1021/jp411382r.

Wang, X., Tamaru, M., Okubo, M., Yamada, A., 2013. Electrode properties of P2-Na2/3MnyCo 1- yO2 as cathode materials for sodium-ion batteries. J. Phys. Chem. C 117 (30), 15545–15551. http://dx.doi.org/10.1021/jp406433z.

Wang, P.F., You, Y., Yin, Y.X., Guo, Y.G., 2018. Layered oxide cathodes for sodium-ion batteries: Phase transition. Air Stability, and Performance, Adv. Energy Mater. 8 (8), 1–23. http://dx.doi.org/10.1002/aenm.201701912.

Whittingham, M.S., 1978. Chemistry of intercalation compounds: Metal guests in chalcogenide hosts. Prog. Solid State Chem. 12 (1), 41–99. http://dx.doi.org/10.1016/0079-6786(78)90003-1.

World Energy Council, 2022. World Energy Trilemma Index 2022. World Energy Council, Olyver Wyman, pp. 1–46.

Yabuuchi, N., Komaba, S., 2014. Recent research progress on iron- and manganese-based positive electrode materials for rechargeable sodium batteries. Sci. Technol. Adv. Mater. 15 (4), http://dx.doi.org/10.1088/1468-6996/15/4/043501.

Yabuuchi, N., Yano, M., Yoshida, H., Kuze, S., Komaba, S., 2013. Synthesis and electrode performance of O3-type NaFeO 2 -NaNi 1/2 Mn 1/2 O 2 solid solution for rechargeable sodium batteries. J. Electrochem. Soc. 160 (5), A3131–A3137. http://dx.doi.org/10.1149/2.018305jes.

Yabuuchi, N., et al., 2012a. P2-type Nax [Fe1/2 Mn1/2[O2 made from earth-abundant elements for rechargeable NaÂ batteries. Nat. Mater. 11 (6), 512–517. http://dx.doi.org/10.1038/nmat3309.

Yabuuchi, N., et al., 2012b. P2-type Nax [Fe1/2 Mn1/2[O2 made from earth-abundant elements for rechargeable NaÂ batteries. Nat. Mater. 11 (6), 512–517. http://dx.doi.org/10.1038/nmat3309.

Yamada, Y., Wada, K., Kagomiya, I., Kakimoto, K., Ohsato, H., 2007. Soft-chemical reaction of layered perovskite Na2Nd2Ti3O10 and its microwave dielectric properties. J. Eur. Ceram. Soc. 27 (8-9 SPEC. ISS.), 3049–3052. http://dx.doi.org/10.1016/j.jeurceramsoc.2006.11.028.

Yang, Z.(Gary), 2011. Electrochemical energy storage for green grid: Status and challenges. In: ECS Meeting Abstracts, Vol. MA2011-02, No. 4. pp. 155–155. http://dx.doi.org/10.1149/ma2011-02/4/155.

Yang, Q., et al., 2018. Advanced P2-Na2/3Ni1/3Mn7/12Fe1/12O2 cathode material with suppressed P2-O2 phase transition toward high-performance sodium-ion battery. ACS Appl. Mater. Interfaces 10 (40), 34272–34282. http://dx.doi.org/10.1021/acsami.8b12204.

Yazami, R., Touzain, P., 1983. A reversible graphite-lithium negative electrode for electrochemical generators. J. Power Sources 9 (3), 365–371. http://dx.doi.org/10.1016/0378-7753(83)87040-2.

Yoshida, H., Yabuuchi, N., Komaba, S., 2013. NaFe0.5Co0.5O2 as high energy and power positive electrode for Na-ion batteries. Electrochem. Commun. 34, 60–63. http://dx.doi.org/10.1016/j.elecom.2013.05.012.

Yuan, D.D., Wang, Y.X., Cao, Y.L., Ai, X.P., Yang, H.X., 2015. Improved electrochemical performance of Fe-substituted NaNi0.5Mn0.5O2 cathode materials for sodium-ion batteries. ACS Appl. Mater. Interfaces 7 (16), 8585–8591. http://dx.doi.org/10.1021/acsami.5b00594.

Yuan, D., et al., 2014. P2-type Na0.67Mn0.65Fe0.2Ni 0.15O2 cathode material with high-capacity for sodium-ion battery. Electrochim. Acta 116, 300–305. http://dx.doi.org/10.1016/j.electacta.2013.10.211.